

Accelerator Facility

Top-up Injection Test

Top-up injection scheme will be adopted in the NSRRC future operation and we have run several shifts of top-up mode with potential users and promising results are obtained. Some of the sub-system improvements are listed below and detailed report is given in the Facility Highlights section by G. H. Luo.

(a) Injector performance improvement

Major improvements of the injector includes components reliability upgrade and improvements and quick replacements of the spare parts of the power supplies, microwave signal monitoring of the preinjector system, and diagnostics upgrade for both preinjector and booster synchrotron. The resonance charging scheme of the klystron modulator in the 50 MeV linac of the preinjector system have been changed to command charging. A new switching power supply is adopted for the pulse forming network and, as a result, much better performance of the modulator is demonstrated. Power supplies for injection and extraction kickers, bumpers and septum will be upgraded. For simplicity and reliability the original Bitbus network for these devices will be replaced by the VME crate system. A standby and fast switching system of quadrupole DC&AC power supplies has been assembled and a similar system for dipole power supply will be implemented as well. We have upgraded DCCT, betatron tune monitor, gated synchrotron radiation monitor, etc. New synchrotron radiation monitor

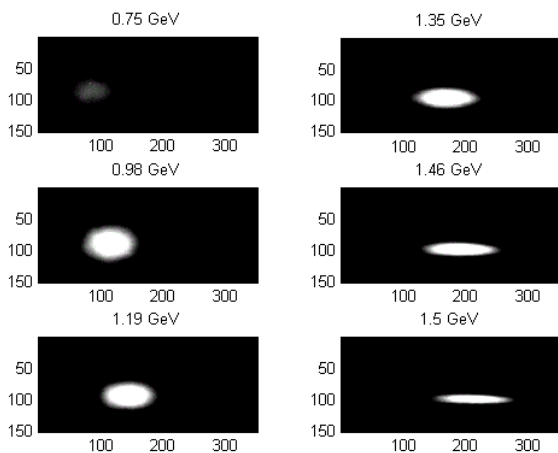


Fig. 1: An example of observed beam profile during the ramping at different energy (pixel size with 2x2 binning: 9.4 μm ., exposure time: 0.5 msec).

have been set up by using the latest version of IEEE1394 digital camera. Gated profile measurement can be easily obtained, and delay time and exposure time can be remotely controlled. A typical measurement result is given in Figure 1.

(b) Low jitter kicker power supply development for the storage ring injection

A prototype air-cooled kicker power supply of the storage ring has been built and the timing jitter of the output pulse current has achieved an excellent level of 3 ns peak-to-peak as shown in Figure 3. This is a large improvement from the existing operating kicker of ~ 25 ns peak-to-peak (Figure 2). The orbit perturbation during injection

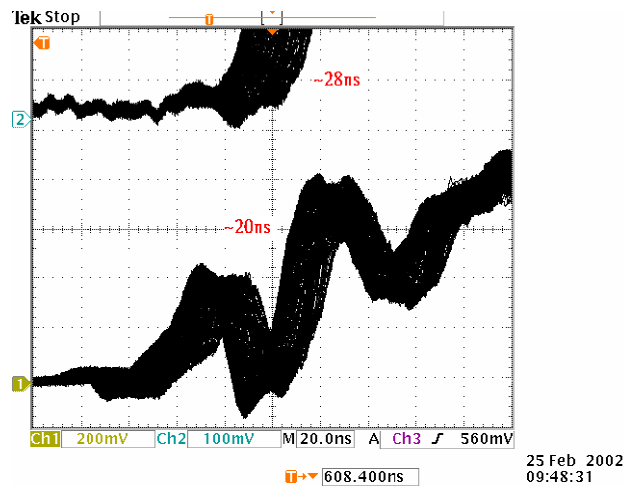


Fig. 2: Typical kicker jitter of the existing kicker pulser.

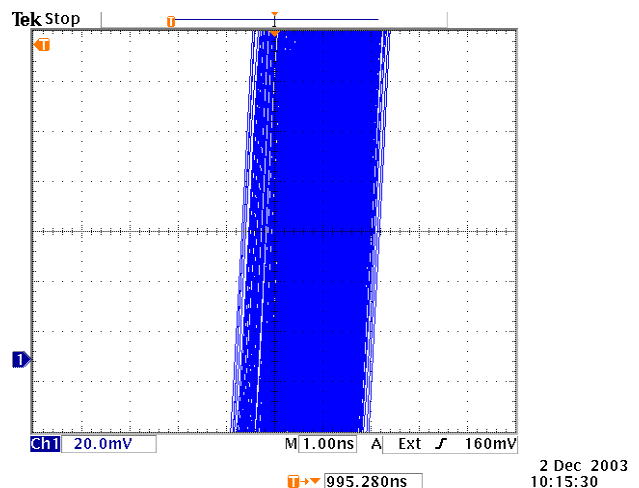


Fig. 3: 3 Kicker jitter of the prototype kicker pulser.

as well as the injection efficiency in the top-up mode could be optimized.

Beam Orbit Stability

(a) Orbit feedback system upgrade

A new architecture of the orbit feedback system is implemented. The DSP was replaced by a new generation G4 PowerPC general-purpose processor which utilizes the AltiVec engine to perform parallel processing of multiple data elements (SIMD) with 128-bit operations. The AltiVec processor executes both fixed- and floating-point instructions, augmenting the separate integer and floating-point units on the chip. The feedback processor is installed in an independent VME64x crate which provides a convenient environment for system development and maintenance. New system is capable of handling sufficient computer power to accommodate more BPMs and correctors in the feedback loop. Sophisticated control rule is to improve the performance and real-time diagnostics of the feedback loop is also supported.

(b) Digital beam position monitor test bed integration

A test bed of digital receiver based beam position monitor (DBPM) is implemented. The system composes a multi-channel coherent down-converter and a VME64x crate is equipped with a multi quad-digital receivers board (QDR). Preliminary results show that the system can achieve a sub-micron resolution in closed-orbit mode and better than 20 μm resolution in turn-by-turn mode. Figure 4 shows

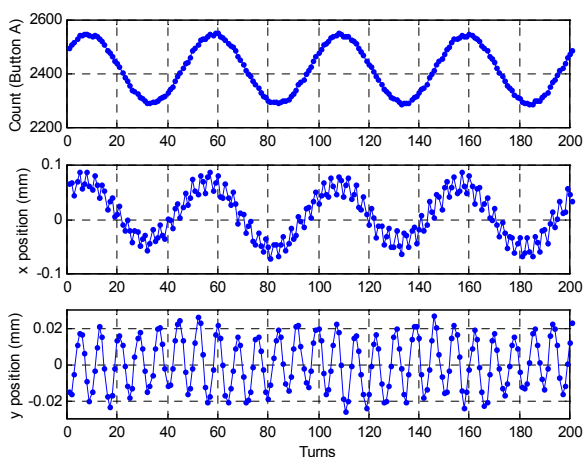


Fig. 4: Preliminary results of the DBPM test bed show that the turn-by-turn resolution is better than 10 μm . Upper: single button signal; Middle: non-calibrated horizontal position; Bottom: non-calibrated vertical position.

the preliminary turn-by-turn data for one DBPM with white noise. The upper figure is a single button signal. The prominent sinusoidal signal is induced by the RF gap voltage modulation. Turn-by-turn beam position is calculated by using four button signals. Middle figure shows that the horizontal position rides on the 50 kHz background. This background is due to non-calibration of the four button processing chain. Parallel processing electronics are insensitive to the longitudinal instability in principle. The background can be minimized after proper calibration. Bottom figure is the vertical position which shows clean betatron oscillation. Estimated resolution for the turn-by-turn mode is better than 20 μm .

(c) Magnet girder assembly

In order to install three IASW6 superconducting wigglers in the arc sections of the storage ring, corresponding girders have to be renewed. Together with the requirements for increasing the stiffness of the girder to have a low vibration response, a prototype girder was developed (Fig. 5). The girder is designed with the following features: 1) composite damping material (CDM) is adopted for vibration suppression; 2) the BPM fixture has a much higher stiffness in transverse direction than in longitudinal direction; 3) the pedestal can be filled with water to keep thermal stability; and 4) a fine adjusting mechanism with four points supporting. The testing results of the girder show a good performance in the frequency response. The natural frequency locates at 35 Hz of a quadrupole on the girder (Fig. 6). The frequency is about two times higher than that of the old girder.

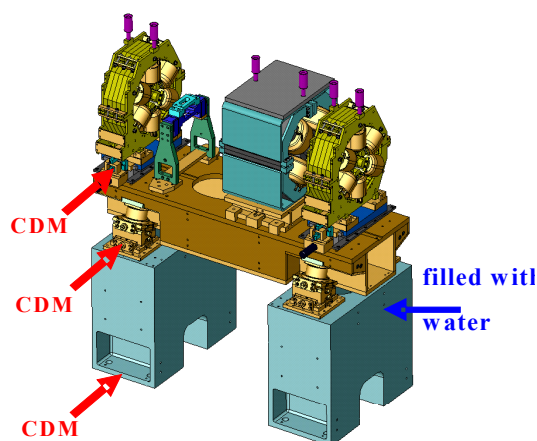


Fig. 5: Low vibration response prototype girder.

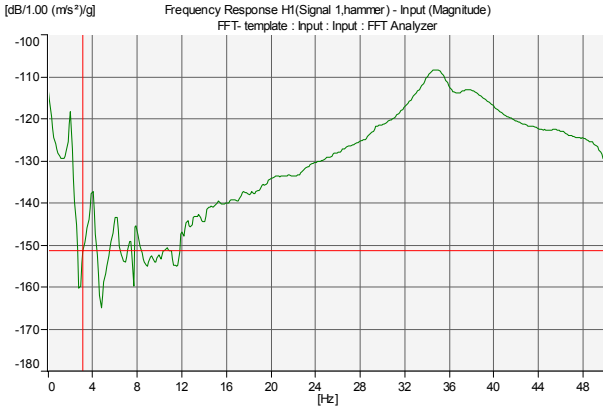


Fig. 6: Results of the girder frequency response.

Beam Instabilities

(a) Effect of RF cavity temperature variation on electron beam with RF voltage modulation

It was observed at NSRRC that a variation of 0.5°C in the peak-to-peak RF cavity (Doris-type) body temperature can induce a 3% variation in the horizontal beam size, measured by a synchrotron light monitor using a CCD camera from a dispersive location. This experiment sets a tight limit of the cavity cooling-water temperature control, which has attained the accuracy of ±0.1 °C. We analyzed this phenomenon and show that it is related to the combined effects of cavity frequency shift, the change of effective accelerating voltage resulting from the partially compensating low-level RF feedback system, and the RF voltage modulation used to combat the coupled bunch instability.

(b) Ion instability

Other than severe longitudinal coupled-bunch instability (LCBI) generated by the higher-order modes of the Doris-type cavities, there exists troublesome transverse ion instability after installing a superconducting wavelength shifter SWLS and a new narrow gap vacuum chamber for the superconducting wiggler SW6. The LCBI can be suppressed by the careful adjustments of the cavity temperature, second plunger tuner and voltage modulation. We have tried several methods to cope with the ion instability such as increasing chromaticities, leaving longer empty bucket train and using feedback damping system. Of course, to improve the vacuum condition is a necessary solution and, for this purpose, some projects are currently carried out in the vacuum group. To ease the routine operations, at present, a longer empty bucket filling pattern has been an acceptable solution.

Superconducting RF

(a) System integration status

The transmitter for the SRF basically is similar to the existing RF transmitter. We are now able to operate the new transmitter up to 100 kW output. An identical low level RF system will be used for controlling the phase and amplitude of the gap voltage. In addition, a direct feedback system has been implemented in such system in order to reduce beam loading effect in the SRF cavity. In order to provide 3MV RF peak voltage for the conditioning of the SRF cavity, a high power WR1800 magic-T to combine the output RF power of the two existing transmitters will be employed. The cryogenic distribution box and its controller have been successfully tested and the result shows that the distribution box works well. Detailed status report of the SRF project is given by Chaoen Wang in the Facility Highlight section

(b) Evaluation of the Impedance for Superconducting RF Cavity

The evaluation of the impedance spectrum for the SRF cavity was carried out by using a parallel simulation program GdfidL. The model complicates the computer simulation but allows us to take into account the reality. The calculated cutoff frequencies of waveguide modes are 4.712 GHz and 2.237 GHz for the longitudinal and transverse planes, respectively, for the elliptical beam pipe. The impedance spectrum is calculated from the Fourier transform of wake potentials. The ferrite properties at 4.75 GHz are used for the worst case analysis. The longitudinal impedance of SRF module is shown in Fig. 7. This longitudinal coupled-bunch instability is not expected to occur at a beam current of 400 mA.

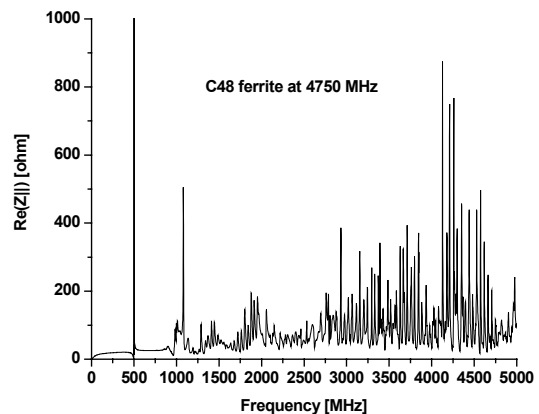


Fig. 7: The longitudinal impedance of SRF module calculated by GdfidL. The cutoff frequency of waveguide modes in the elliptical beam pipe is 4.712 GHz.

Superconducting Wigglers

(a) Superconducting wiggler SW6

A 6 cm-period superconducting wiggler (SW6), with 28 effective poles (totally 32 poles) and peak field strength 3.2 T, was constructed and installed in the storage ring (Fig. 8). A peak field of 3.2 T was obtained at an excitation current of 285 A. The SW6 has been successfully commissioned with beam, April 26, 2004. Detailed report is given by C. S. Hwang in the Facility Highlights section.

(b) Vacuum beam duct

The vacuum beam duct of the SW6, operated at a low temperature of ~ 100 K, was developed. The A6061T5 aluminium alloy was adopted as the material for the beam duct due to the benefit of lower radiation emissivity and easy fabrication. The beam duct is made by extrusion method and machined on outside surfaces afterwards to obtain a high precision

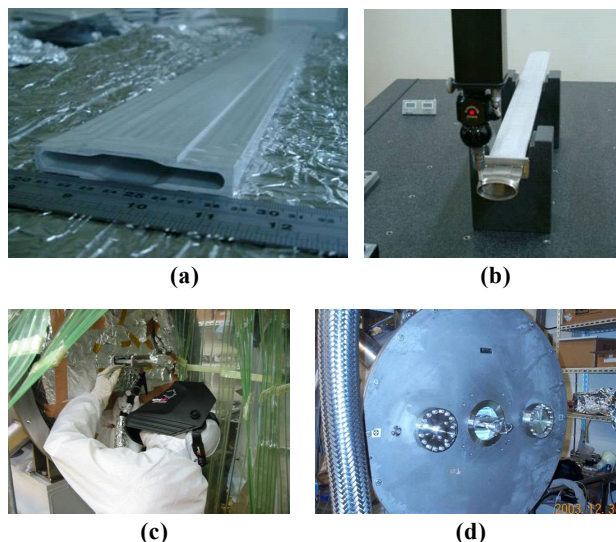


Fig. 10: Photographs of (a) Al beam duct, (b) flatness check for Al beam duct, (c) on-site TIG welding for the taper, and (d) the completed beam duct on SW6.



Fig. 8: The superconducting wiggler SW6 installed in the storage ring.

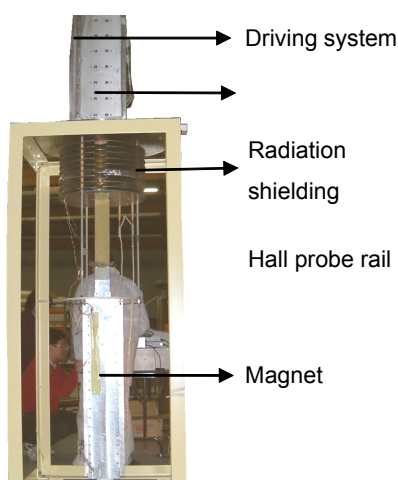


Fig. 9: Field measurement system on the vertical dewar to measure field distribution on three axis of $x=0, \pm 20$ mm.

of flatness < 0.2 mm so that the chamber can be inserted inside the magnetic poles without touching the 4 K insulation vacuum vessel. The stainless steel (SS) tapers on both ends of the beam duct, connected by TIG-welding Al/SS bimetals, play a role of cold-warm transition tubes. Figure 10 illustrates the photographs of (a) Al beam duct, (b) flatness check for Al beam duct, (c) on-site TIG welding for the taper, and (d) the completed beam duct on SW6. A chamber has been tested, at both room temperature and low temperature at 100 K, in the 19B1/PSD photon beam line. Figure 11 shows the log-log plot for the photo-desorption yield, η (molecules/photon), as a function of the beam dose. The figure depicts the

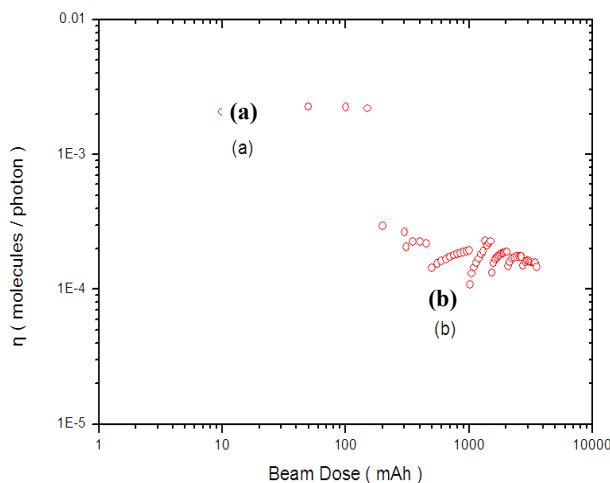


Fig. 11: The photo-desorption yield (η) vs. beam dose. The circles in the plot depict the η at a region around room temperature (a) and at a region around cryogenic temperature of 100 K (b).

η value at a region around room temperature (η -warm) (a) and the η value at a region around cryogenic temperature of 100 K (η -cool) (b). The trend of both the η -warm and η -cool are not decreasing as beam dose increasing. It seems that the rate of beam cleaning is not efficient.

(c) SW6 control system integration

Control system for SW6 coordinates the operation of the main power supply and the trim power supplies for the magnet charging and discharging processes and provides the essential magnet interlock protection mechanisms. A local controller is a VME crate-based system with a PowerPC CPU module running LynxOS real time operating system. Standard RS-232 interface is used for the communication among various cryogenics instruments and power supplies. A programmable logic controller is employed for the interlock logic. The layout of the control rack for SW6 is shown in Figure 12, and a graphical user interface supports the routine operation as in Figure 13. A number of application software programs have also been developed to facilitate the operation of the SW6.

Synchrotron Radiation Interferometer Beam Size Monitor

A new beam size monitoring system based on the synchrotron radiation interferometer was installed in the beamline BL10B. This system consists of a water-cooled beryllium mirror, a double slits, focus optics and CCD detectors. The optical layout of the monitor is shown in Fig. 14. A preliminary result is shown in Fig. 15. The synchrotron radiation interferometer beam size monitor system is capable of micron accuracy and sub-micron resolution.

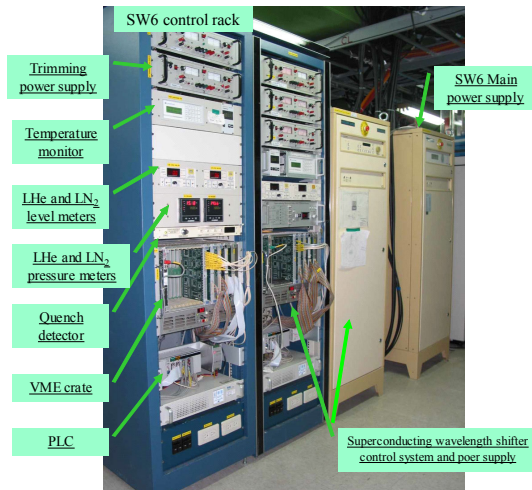


Fig. 12: Control rack and the power supply for the SW6.

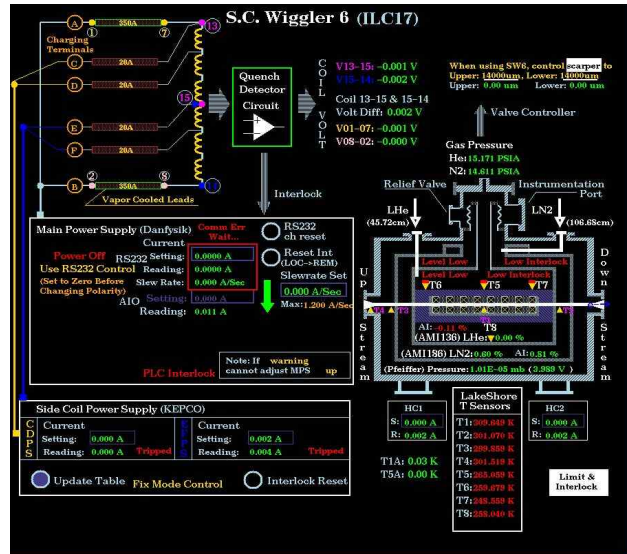


Fig. 13: Graphical user interface for the SW6.

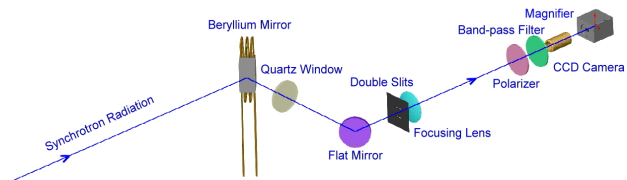


Fig. 14: The optical path of the synchrotron radiation interferometer beam size monitor system.

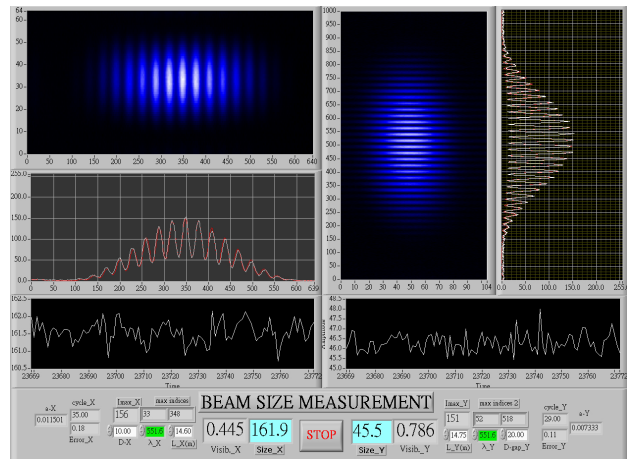


Fig. 15: Result of the synchrotron radiation interferometer beam size monitor.

Cryogenics System

The first cryogenic system, to supply liquid helium to the SRF cavity, finished its commission phase in the year 2003. After commissioning, the system is demonstrated to have the capacity supporting four different operation modes:

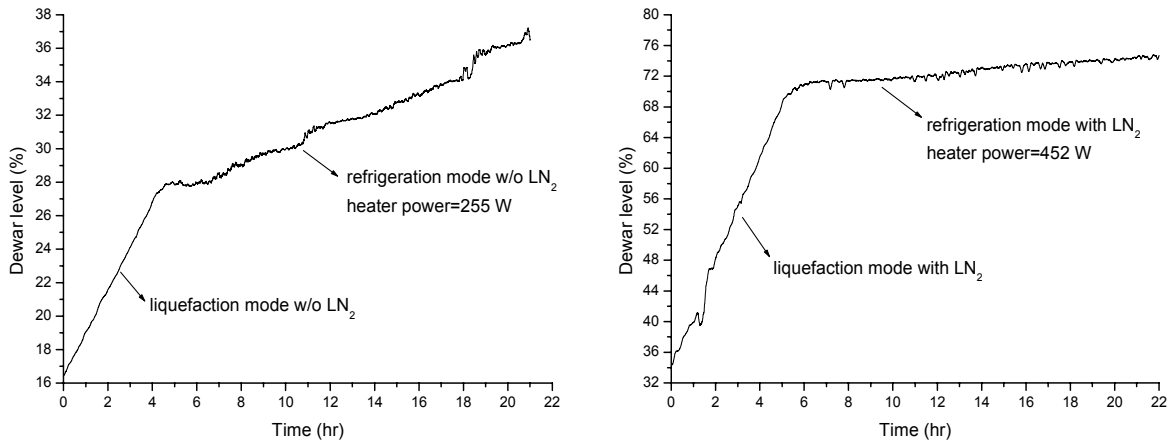


Fig. 16: Capacity measured at main dewar.

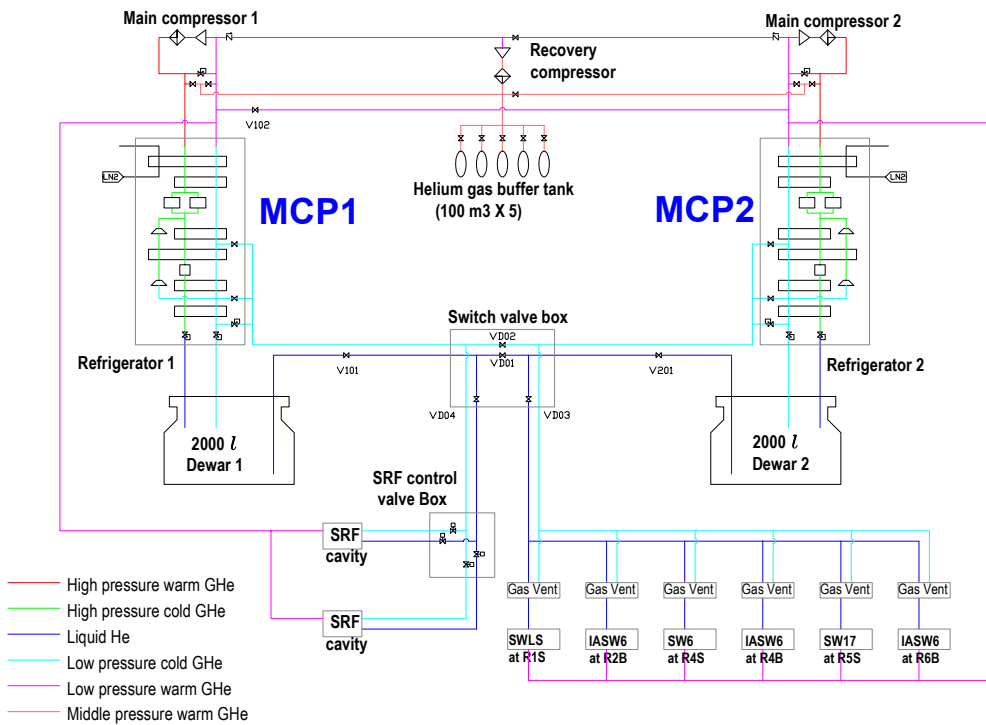


Fig. 17: Flow diagram of two cryogenic systems.

- (1) The helium liquefaction rate is 52 l/hr without liquid nitrogen for precooling.
- (2) The helium liquefaction rate is 134 l/hr with liquid nitrogen for precooling.
- (3) The cooling power is 258 W at 4.5 K without liquid nitrogen for precooling.
- (4) The cooling power is 452 W at 4.5 K with liquid nitrogen for precooling.

The system also demonstrated its stable operation with a pressure fluctuation of +/-2 mbar at the suction end of the compressor and a pressure fluctuation of +5/-3 mbar at the liquid helium

storage dewar. Figure 16 presents the test results. The second cryogenic system is designed for the superconducting wigglers in the storage ring and also as a backup system of the SRF cryogenic system. Figure 17 shows the flow chart connecting the two systems. The capacity of the second system is similar to the first one but with an additional requirement on mix-mode operation of minimum.

The specifications for the main system (liquid helium production) and the distributing system (liquid helium/nitrogen transfers) were fixed and the contracts for these two systems were signed with

MACHINE STATUS

the vendors in 2003. The interconnect piping, for the discharge line and quench return line, and a storage gas tank were manufactured and installed. The whole systems associated with an external purifier system are scheduled to be ready in the year 2005.

AUTHORS

K.-T. Hsu, J.-R. Chen, and C.-C. Kuo
National Synchrotron Radiation Research Center,
Hsinchu, Taiwan

CONTACT E-MAIL

cckuo@nsrrc.org.tw